Supplementary Information (SI) for Energy & Environmental Science.

Supplementary Information

Interfacial solar evaporation-driven lithium extraction from salt-lake brines for battery-grade Li_2CO_3 production

Wenqian Xing,[a] Deyu Wang,[b] Kai Feng,[a] Shihao Ding,[a] Xinle Zhang,[a] Haolan Xu,*[b] Jiang Gong,*[a] Jinping Qu,[a] Ran Niu*[a]

[a] Key Laboratory of Material Chemistry for Energy Conversion and Storage, Ministry of Education, Hubei Key Laboratory of Material Chemistry and Service Failure, Hubei Engineering Research Center for Biomaterials and Medical Protective Materials, School of Chemistry and Chemical Engineering, Huazhong University of Science and Technology, Wuhan 430074, China.

[b] Future Industries Institute, UniSA STEM, University of South Australia, Mawson Lakes Campus, Adelaide SA 5095, Australia

*Corresponding authors

E-mail address: haolan.xu@unisa.edu.au; gongjiang@hust.edu.cn; niuran@hust.edu.cn

Table of content

Experimental Section

1. Chemical and materials

Polyvinyl alcohol (PVA-1799, 98-99% hydrolyzed) was purchased from Aladdin Reagents (China). Brine was collected from East taigener salt-lake (Qinghai, China). Glutaraldehyde, HCl (37%), NaCl, ferric sulfate ($Fe_2(SO_4)_3$), Tannic acid (TA) were purchased from Sinopharm Chemical Reagent Co. Ltd (China). Tris(hydroxymethyl) methylaminomethane (Tris, 99%), (3-aminopropyl) triethoxysilane (APTES), octadecyltrimethoxysilane (OTS), ethanol, Rhodamine B (RhB), methyl blue (MB) and other chemicals were obtained from Sigma Aldrich (USA). Carbon black (CB) with a diameter of 30-45 nm was received from XFNANO Materials Tech Co. Pristine sponge was purchased from Shanghai Yuxinsheng Trading Co (China). Li_2TiO_3 was purchased from Macklin (China). 2% Sheep erythrocyte solution was purchased from Sablib (China). 1×PBS solution was received from Solarbio (China). Nitric acid (HNO_3, 65–70%), hydrofluoric acid (HF, 40%) and hydrogen peroxide (H_2O_2, 30%) were purchased from Sigma-Aldrich.

2. Characterization

The mechanical properties of hydrogels were assessed by a Universal Tensile Testing Machine (SUNS UTM5000, China). The light absorption performance in the wavelength range of 500 to 2500 cm was characterized by an UV6400 spectrophotometer. A thermal conductivity analyzer (Hot Disk, TPS 2500) was used to measure the thermal conductivity of materials. Contact angle (CA) and rolling angle (RA) of water on the sample surface were characterized using an automatic CA testing apparatus (OCA 40, Data Physics Corporation, Germany). A high-speed camera (UX100, Photron) was used to perform droplet impact tests. The microstructure and composition of the samples were characterized using a scanning electron microscope (SEM, ESCAN MIRA LMS) equipped with energy dispersive spectrometry (EDS). Element composition was analyzed via X-ray photoelectron spectroscopy (XPS, Thermo ESCALAB 250XI). Identity of the H_2TiO_3 was confirmed by X-ray diffraction analysis (XRD, Rigaku, Japan). Additionally, lithium concentration in adsorption or desorption experiments and metal ion concentration in competitive adsorption experiments were measured using inductively coupled plasma emission spectroscopy (ICP-OES, Thermo Fisher SCIENTIFIC, Germany).

3. Preparation of O-Sponge

(1) Preparation of M-Sponge

0.05 g of TA was added to 25 mL of buffer solution (Tris-HCl, pH= 8.5), followed by addition of ethanol (5 mL) and (3-Aminopropyl) triethoxysilane (APTEs, 0.05 mL). A piece of the rubber sponge (1 cm × 1 cm × 0.3 cm) was immersed in the above solution for 12 h at room temperature. Subsequently, it was washed using distilled water and ethanol respectively and then was placed into 2 mg mL^{-1} of $Fe_2(SO_4)_3$ solution for 4 h to obtain the M-Sponge.

(2) Preparation of O-Sponge

The M-Sponge was immersed in a mixture of ethanol (20 mL), OTS (0.1 g) and deionized water (2 mL) for 16 h. The sponge was then thoroughly cleaned with ethanol to obtain the O-Sponge.

4. Solar-driven evaporation experiments

Indoor solar evaporation performance of the 3D evaporator was evaluated under simulated solar light using a Xenon lamp (300-1100 nm, CELS500L, AULTT, China) as light source. A solar meter was used to calibrate the intensity of the solar flux (CELS500L, AULTT, China). The mass loss of water during solar evaporation was recorded in real time on an electronic balance of 0.1 mg accuracy (JA2003, Soptop). The surface temperature of the evaporator was measured by an infrared camera (DMI220, Dongmei). Water evaporation rate (m, kg m^{-2} h^{-1}) and solar-to-vapor conversion efficiency (η, %) were calculated by following equations:

$$m = \Delta m / \left(S \times t\right) \tag{S1}$$

$$\eta = m' \times h_{LV} / P_{in} \tag{S2}$$

where Δm represents water mass loss (kg) in 1 h; S refers to the evaporator's top surface area of the water-filled hydrogel (i.e., the interface between hydrogel to air); t stands for irradiation time (1 h); m' stands for evaporation rate after subtracting that in the dark; h_{LV} is the enthalpy of vaporization (kJ kg^{-1}), and P_{in} is the illumination intensity (1 kW m^{-2}).

Evaporation in the dark was performed to estimate the evaporation enthalpy of the evaporator using the following equation:

$$m_0 h_0 = m_{eva} h_{LV} \tag{S3}$$

where m_0 and m_{eva} was the measured evaporation rate of pure water and evaporators in dark (kg m^{-2} h^{-1}); h_0 and h_{LV} were the evaporation enthalpy of water and evaporators, respectively.

5. Effect of solution pH on lithium adsorption

The optimal pH for lithium adsorption was investigated by solar evaporation of LiCl solutions (Li^+: 200 ppm, V: 50 mL) of pH values 8.7, 10.0, 11.0, 12.0 and 13 respectively. The pH value was adjusted using HCl (1.2 M) or NaOH (5 M). The concentration of Li^+ before and after adsorption (10 h) were detected from which the adsorption capacity was calculated.

6. Recyclability of lithium adsorption

The reusability of the 3D evaporator was evaluated in brine (Mg^{2+}/Li^+ ratio: 50, salinity: 40 g L^{-1}) to reveal its stability in long-term use. 0.2 M HCl solution was used for the desorption of Li^+ from CCH, and the desorption process proceeds overnight. Then, the eluate was collected, and the lithium concentration was analyzed using ICP-OES. The desorption efficiency was calculated as following:

$$\text{Desorption efficiency} = \frac{C_{des} V_{des}}{C_0 V_0 - C_e V_e} \times 100\% \tag{S4}$$

where C_{des}, C_0, C_e are the lithium concentration in the eluate, original lithium solution, and at adsorption equilibrium, respectively. V_{des}, V_0 and V_e are the volume of desorption solution, lithium solution for adsorption and solution at adsorption equilibrium, respectively. After rinsing the desorbed CCH three time with deionized water, it was ready for the next cycle of lithium adsorption.

The Ti content in the CCH before and after cycled use was measured. First, the CCH was weighed using an analytical balance. A small amount of deionized water was added to wet the sample, followed by the addition of 8 mL nitric acid (HNO_3), 1 mL hydrochloric acid (HCl), and 1 mL hydrofluoric acid (HF). The mixture was then placed in a digestion vessel and subjected to pre-digestion at 120 °C for 30 min, followed by microwave-assisted digestion (TANK40, Sineomicrowave company, China). After cooling to 60 °C, the digested solution was diluted to 25 mL with deionized water. The titanium (Ti) content was determined by ICP-OES.

7. Selective adsorption in simulated solution and real salt-lake brine

The feasibility of 3D evaporator for lithium extraction was tested by dealing with brines of various mass ratios of Mg^{2+}/Li^{+} (Table S7), salinities (Table S8) and simulated three salt-lake brines which contain various ions (Table S2). The adsorption was performed under 1.0 sun irradiation (V= 50 mL) for 10 h. After adsorption, the CCH was washed by deionized water to remove the un-trapped ions. Finally, the Li^{+} in CCH was desorbed by 0.2 M HCl solution (V= 30 mL) within 12 h. The ions concentration in the solution and eluate was analyzed by ICP-OES.

The K_d (mL/g) value and the selectivity (S) were calculated using the following two equations:

$$K_d = \frac{c_{desorb-M} V_{desorb}}{c_{e-M} m} \times 10^3 \tag{S5}$$

$$S = \frac{K_d^{\ Li}}{K_d^{\ M}} \tag{S6}$$

where V_{desorb} is the volume of the eluate (mL), c_{desorb} and $c_{e\text{-}M}$ are the ion concentrations in the eluate and the equilibrium concentration (M is Na^{+}, K^{+}, Ca^{2+} or Mg^{2+}). m is the amount of HTO (mg).

8. Li_2CO_3 collection from elution after simple purification

The eluate can be condensed by solar evaporation using a self-floating hydrophobic O-Sponge to form a saturated solution, which was subsequently adjusted to pH 11 using a saturated NaOH solution to remove any remaining Mg^{2+}. The white precipitate was removed by centrifugation at 1000 rpm for 10 min. Next, saturated sodium oxalate solution was slowly added to the above solution to remove small amounts of remaining Ca^{2+}. The upper clear solution was collected by centrifugation at 1000 rpm for 10 min. Finally, saturated Na_2CO_3 solution was added to the above solution at 80 °C. The white precipitate was collected after centrifugation and dried in an oven at 60 °C for 12 h.

Supplementary Figures

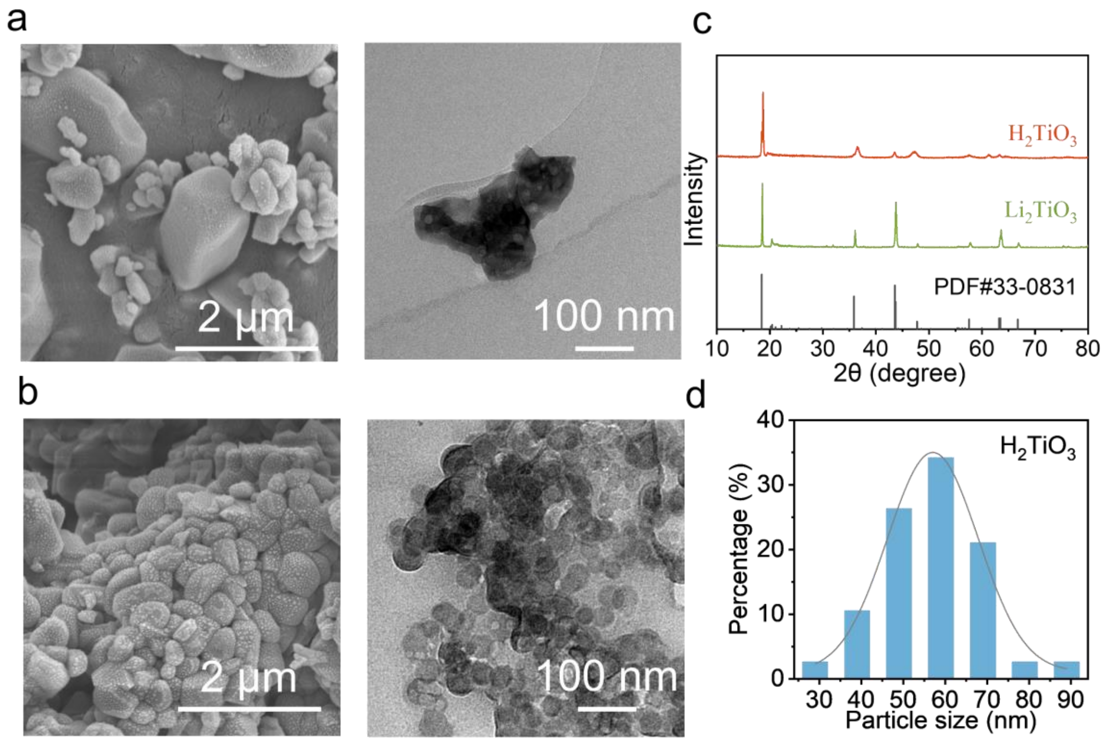

Fig. S1 Characterizations of the H_2TiO_3 and Li_2TiO. SEM images of (a) LTO and (b) HTO. (c) XRD patterns of the prepared H_2TiO_3, Li_2TiO_3 and XRD standard card. (d) Size distribution plot of HTO.

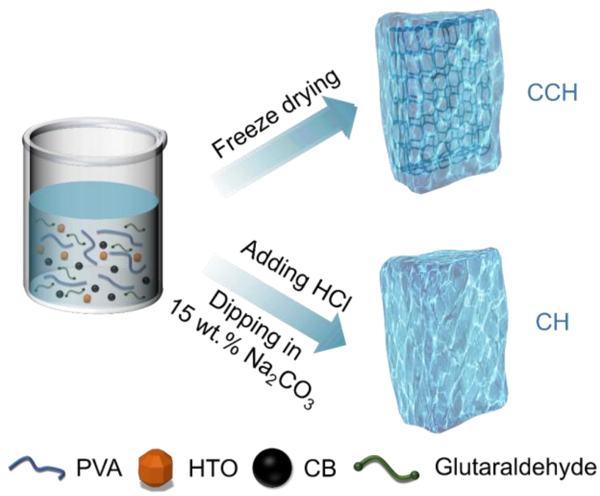

Fig. S2 Schematic illustration of the preparation process for the O-Sponge.

.

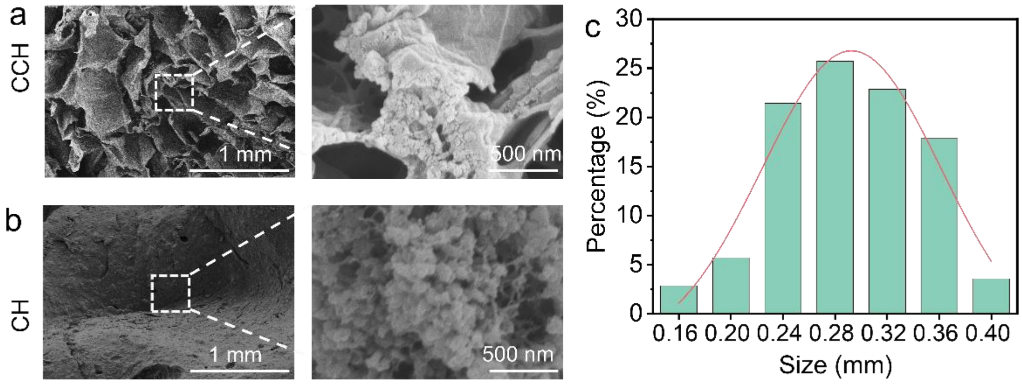

Fig. S3 SEM images of (a) CCH and (b) CH. (c) The pore size distribution of CCH.

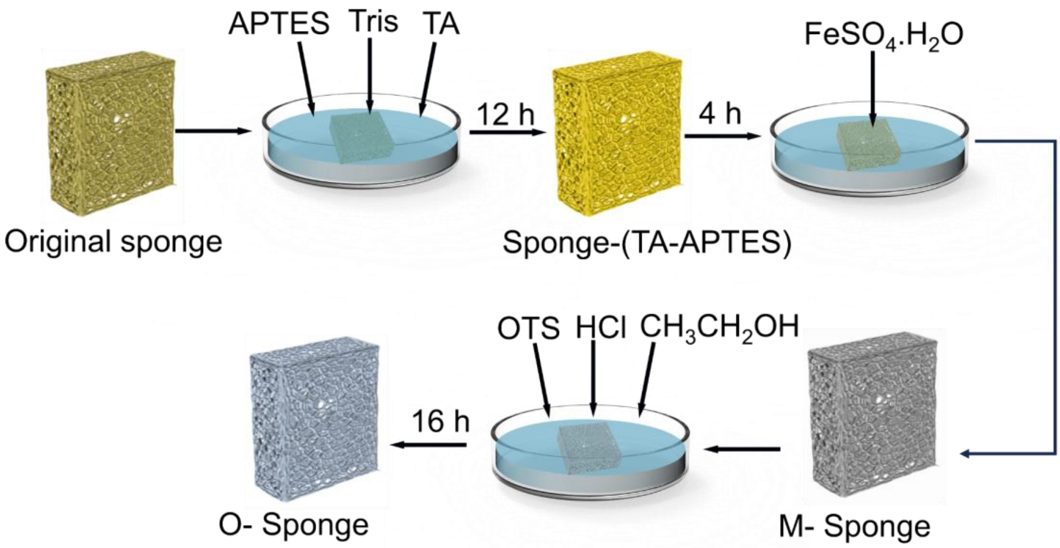

Fig. S4 Schematic illustration of the preparation process for the O-Sponge.

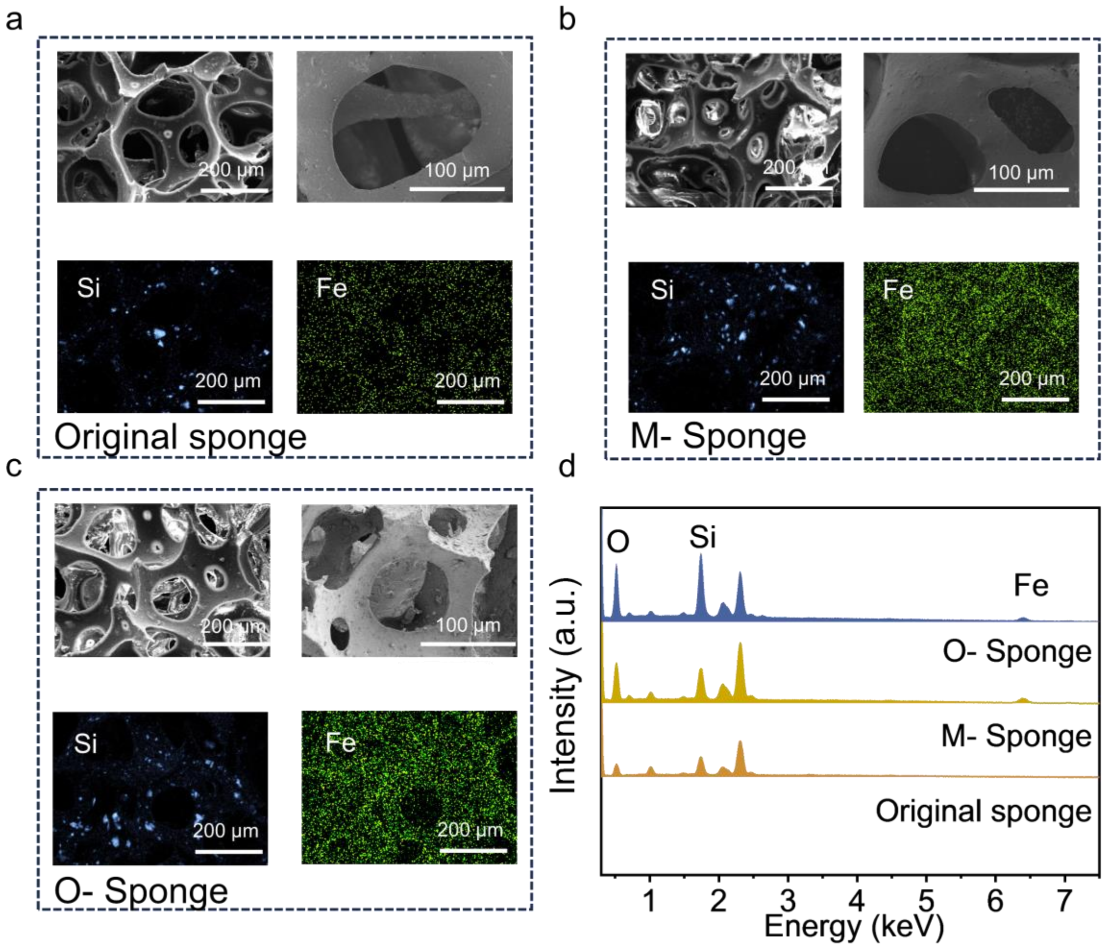

Fig. S5 SEM and EDS mapping images of sponges. (a-c) SEM and EDS mapping images of (a) original sponge, (b) M-Sponge and (c) O-Sponge. (d) EDS spectra of samples.

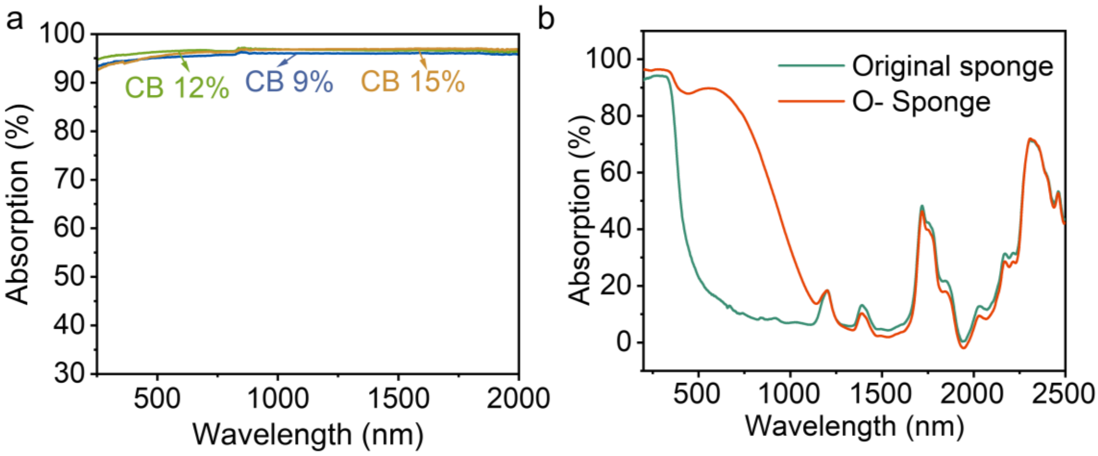

Fig. S6 UV–Vis–NIR spectra of samples. (a) CCH of different CB contents, and (b) original sponge and O-Sponge.

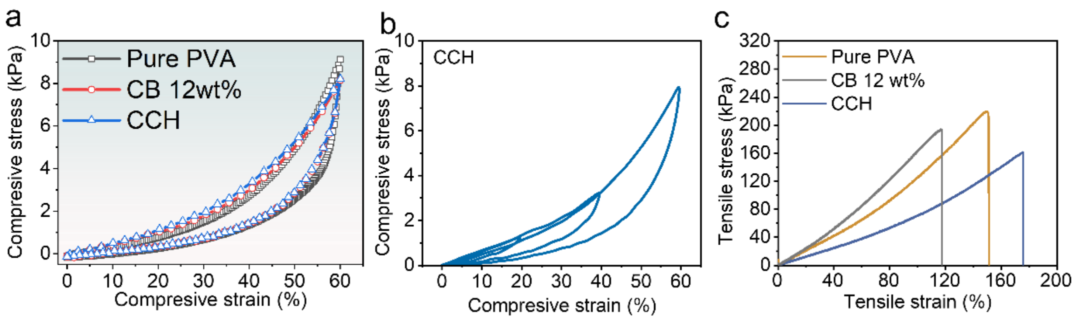

Fig. S7 Mechanical properties of samples. (a) Compressive stress-strain curves of pure PVA, PVA with 12 wt% CB, and CCH. (b) Compressive stress-strain curves of CCH under various compressive strains. (c) Tensile stress-strain curves of PVA, PVA with 12 wt% CB, and CCH.

Fig. S8 Superhydrophobicity of the O-Sponge towards water of various pHs.

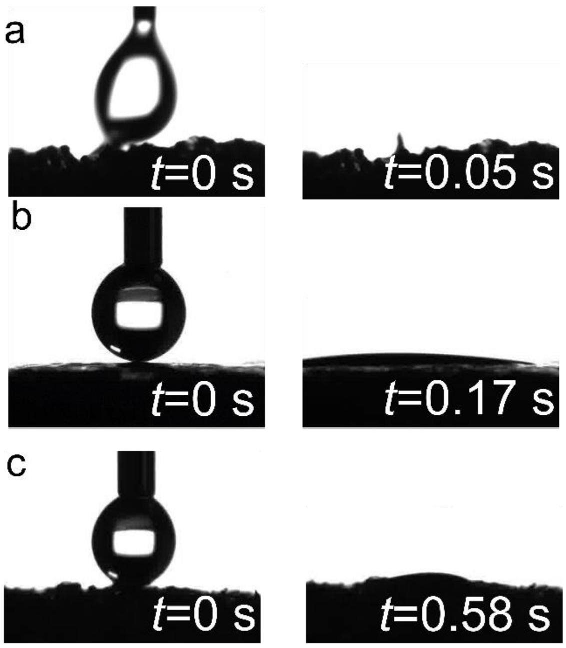

Fig. S9 Water contact angles of (a) CCH, (b) CH and (c) the pristine hydrophilic sponge.

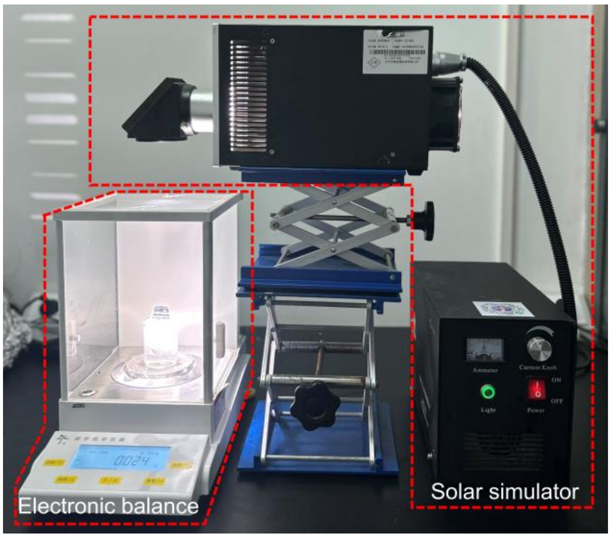

Fig. S10 Photograph of the home-assembled device for indoor solar-driven evaporation and lithium extraction used in this project.

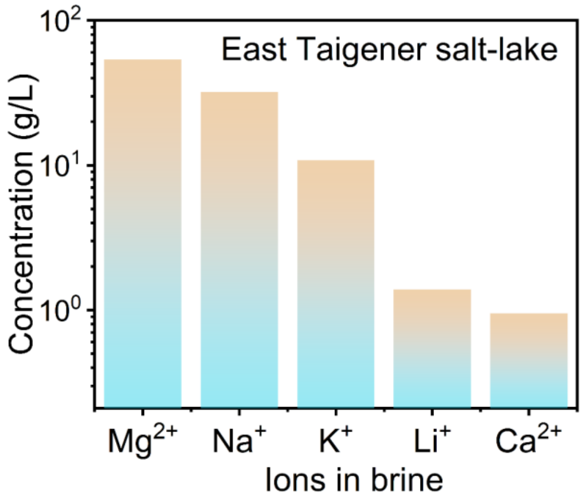

Fig. S11 Composition of East Taigener salt-lake brine.

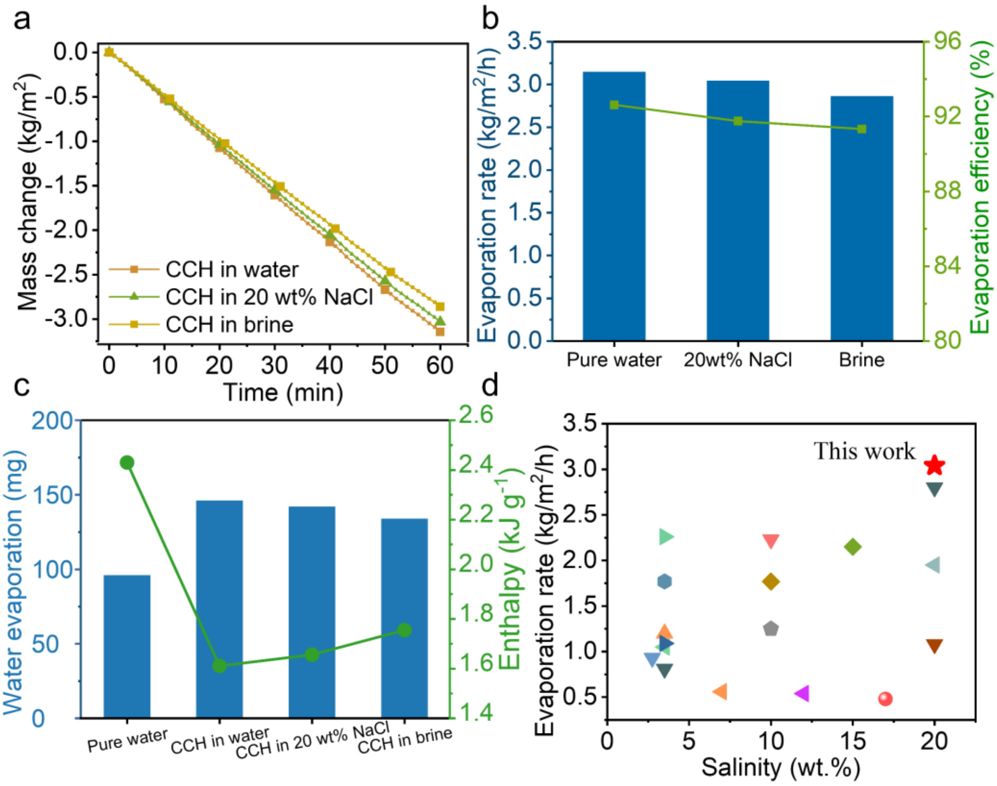

Fig. S12 Evaporation of the 3D evaporator in pure water, NaCl solution and brine. (a) Mass change versus time of the 3D evaporator in various water sources. (b) Evaporation rate and solar-to-vapor conversion efficiency of the 3D evaporator in various water sources. (c) Mass loss of water in the dark during 1 h and the calculated evaporation enthalpy. (d) Solar evaporation performance of the 3D evaporator in salty water of various salinities compared with recent literature (1.0 Sun, see details in Table S1).

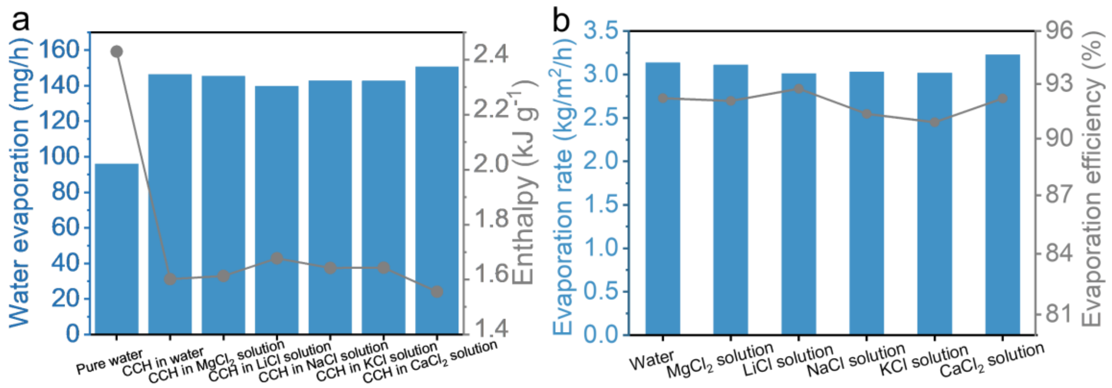

Fig. S13 Evaporation of the 3D evaporator in various waters under dark and 1.0 sun. (a) Water evaporation of pure water and the 3D evaporator in various solutions in the dark and the calculated evaporation enthalpy. (b) Evaporation rate and efficiency of the 3D evaporator in various solutions under solar irradiation of 1.0 Sun.

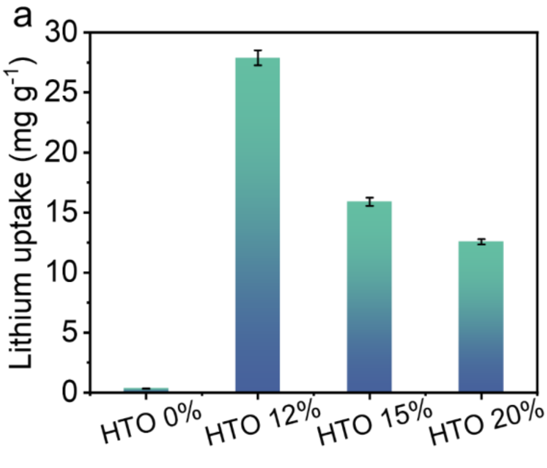

Fig. S14 Lithium uptake condition optimization. (a) Lithium uptake of the 3D evaporator with CCH layer of different HTO contents (c_0= 200 ppm, pH=12). (b) Lithium uptake of the 3D evaporator and evaporator of 0% HTO at different pHs (c_0= 200 ppm).

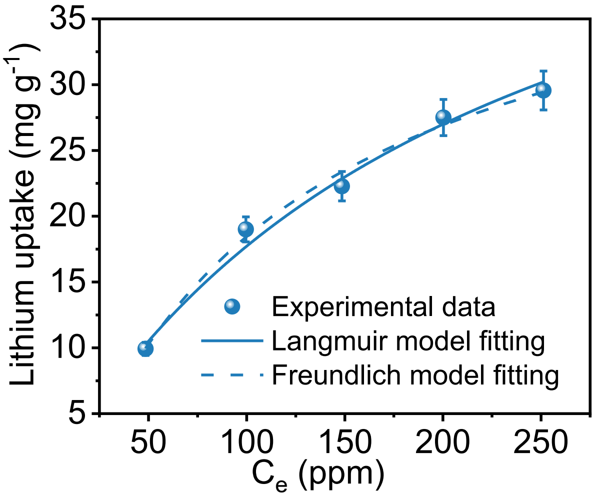

Fig. S15 Isothermal curve of the lithium extraction by the 3D evaporator.

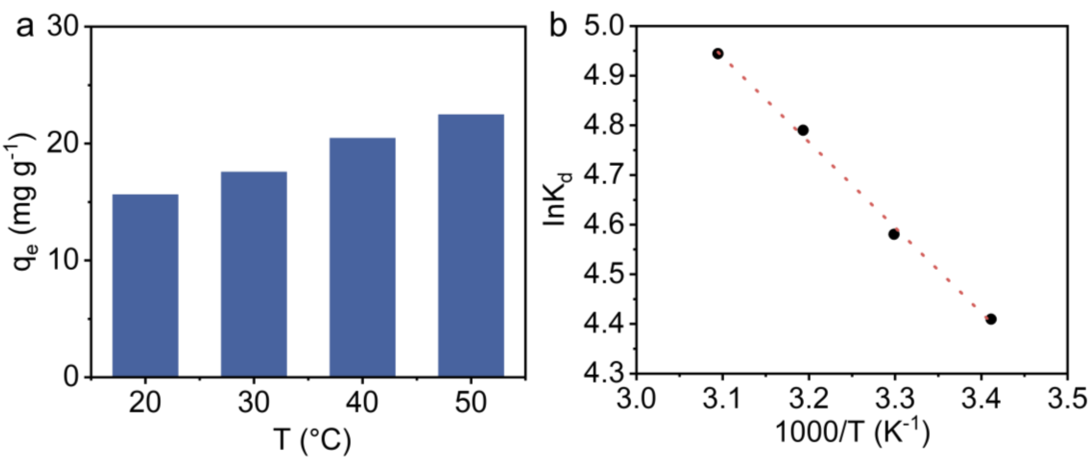

Fig. S16 Adsorption thermodynamics of the 3D evaporator. (a) Equilibrium Li^+ adsorption capacity at different temperatures. (b) Van't Hoff plot for Li^+ adsorption.

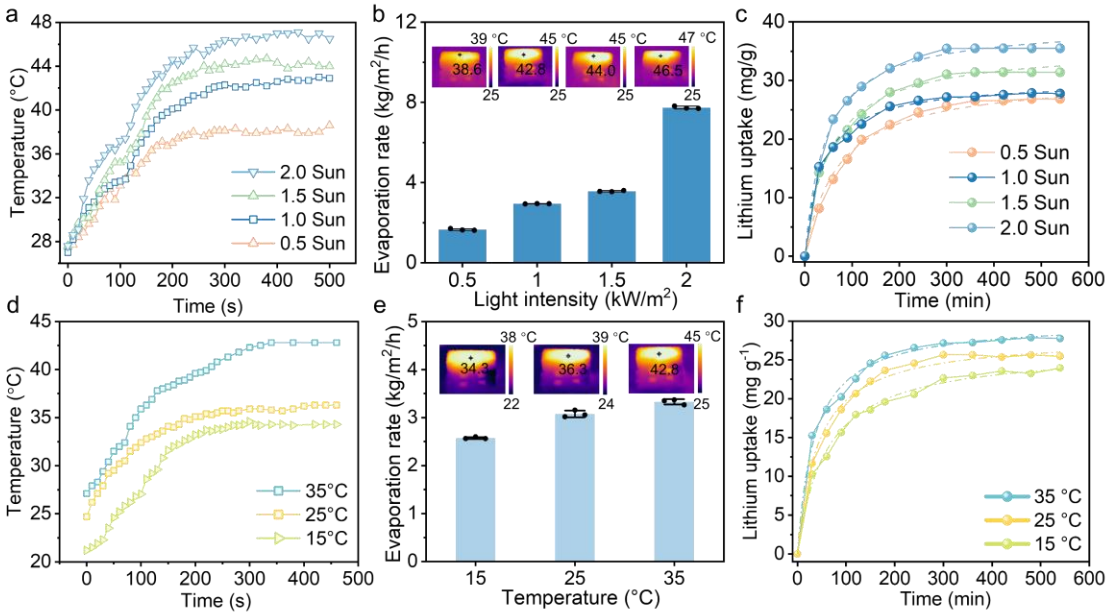

Fig. S17 (a and d) Variation of surface temperature with time under (a) solar irradiation of various intensities and (d) different environmental temperature. (b and e) Evaporation rate and (c and f) lithium uptake of the 3D evaporator under (b and c) solar irradiation of various intensities and (e and f) different environmental temperature.

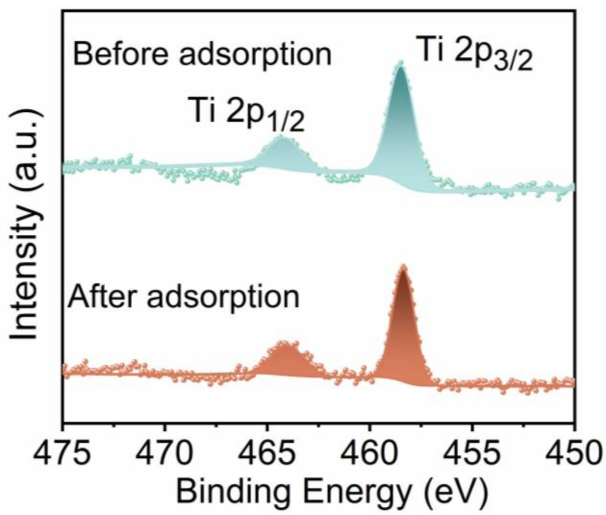

Fig. S18 High-resolution Ti 2p spectra of CCH before and after lithium extraction.

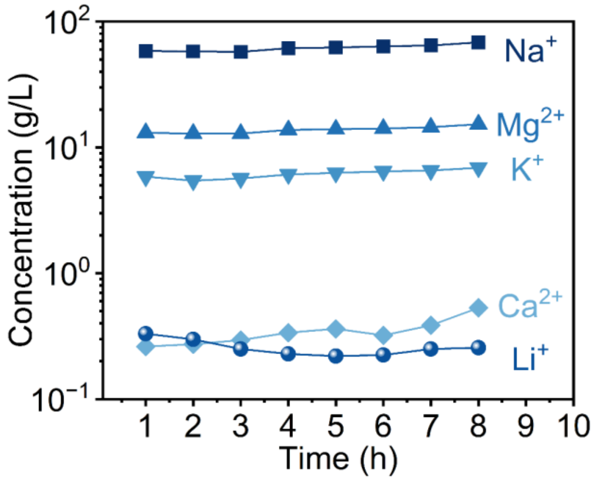

Fig. S19 Composition change of the simulated brine from Chagcam Caka with time during solar evaporation of the 3D evaporator under 1 Sun.

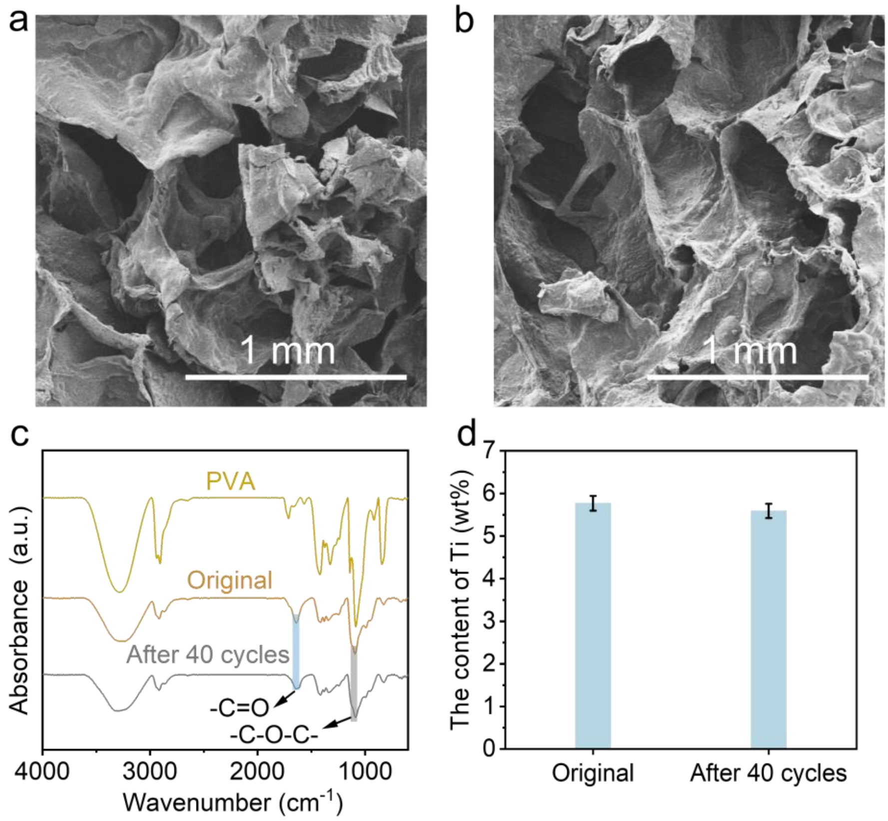

Fig. S20 Stability test of the CCH and HTO after 40 cycles of use. Macroporous structure of the CCH (a) before and (b) after 40 cycles of use. (c) FTIR spectra of PVA, original CCH and CCH after 40 cycles of lithium adsorption from simulate brine. (d) Content of Ti inside the CCH before and after 40 cycles of lithium extraction from simulate brine.

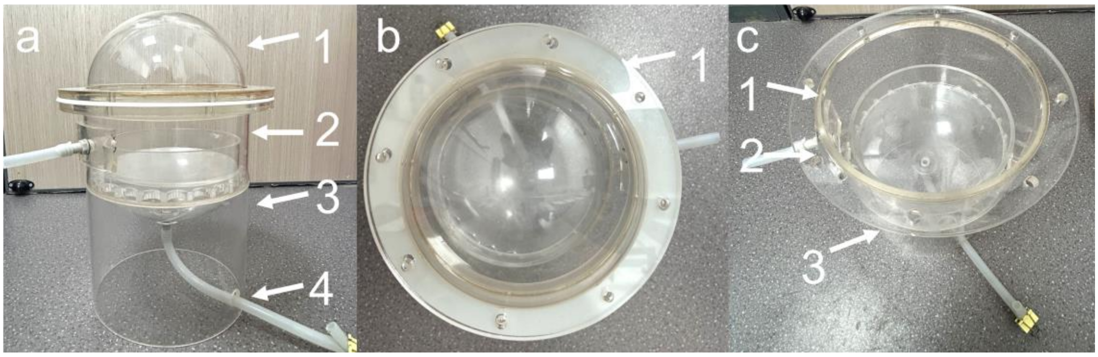

Fig. S21 Photographs of the outdoor solar evaporation device. (a) The whole device, (b) the cover, and (c) the outdoor solar evaporation device without the cover.

Note: (1)-(4) refer to (1) evaporation chamber, (2) steam generation room, (3) supporting plate, and (4) rubber tube, respectively.

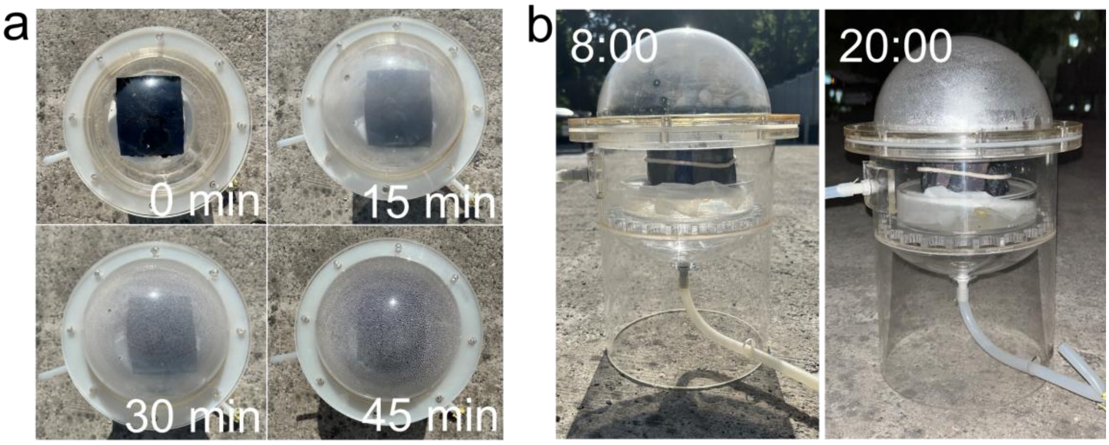

Fig. S22 Photographs of sample in outdoor test. (a) Photographs showing the formation of water droplets on the condenser during the first 45 min in outdoor test. (b) Images of the evaporator at the beginning and end of the outdoor test.

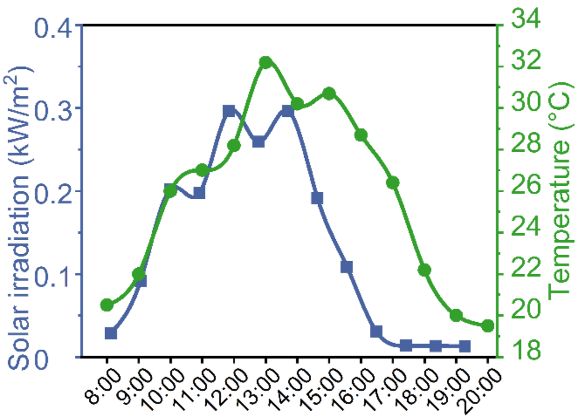

Fig. S23 Fluctuation in solar irradiation and environmental temperature with time during outdoor test.

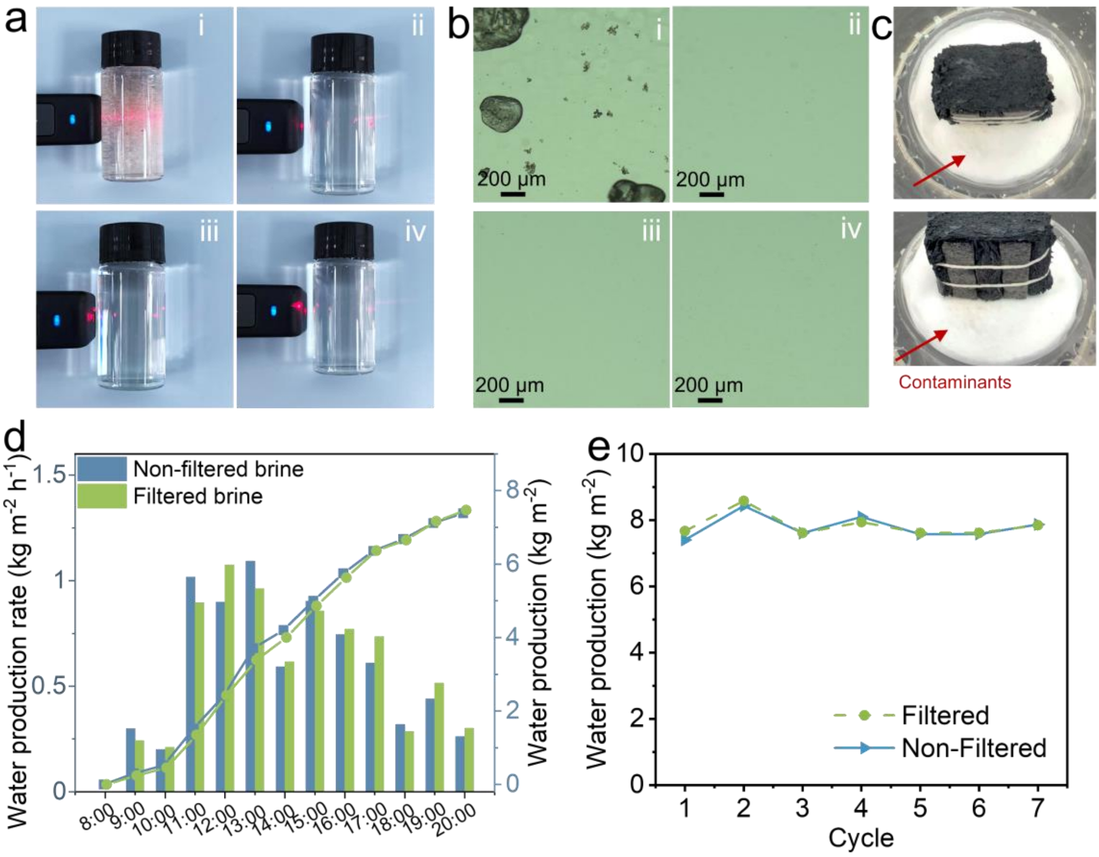

Fig. S24 (a) Digital images and (b) optical microscopy images of the water samples: i non-filtered brine, ii filtered brine, iii desorption solution from i, iv desorption solution from ii. (c) Images of the 3D evaporator after long-time run in non-filtered brine with contaminants on the water conducting paper. (d) Water production rate and accumulated amount during the day when dealing with filter and non-filtered brines. (e) Water production in 7 consecutive days in dealing with filtered and nonfiltered brines.

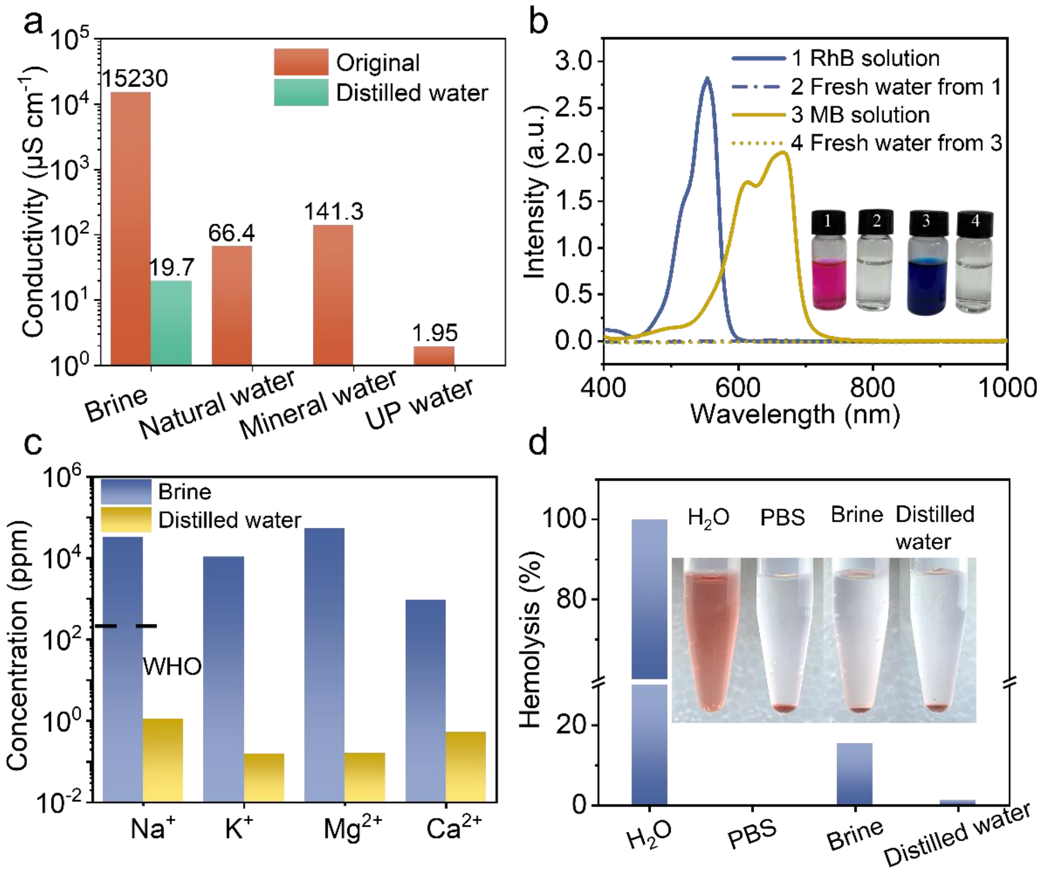

Fig. S25 Quality of the distilled water. (a) Conductivity values of various waters. (b) UV–Vis absorption curves of MB and RhB solutions and the condensed freshwater using 3D evaporator. (c) The ion concentrations of brine before and after desalination. (d) Digital photo and hemolysis ratio of various water samples.

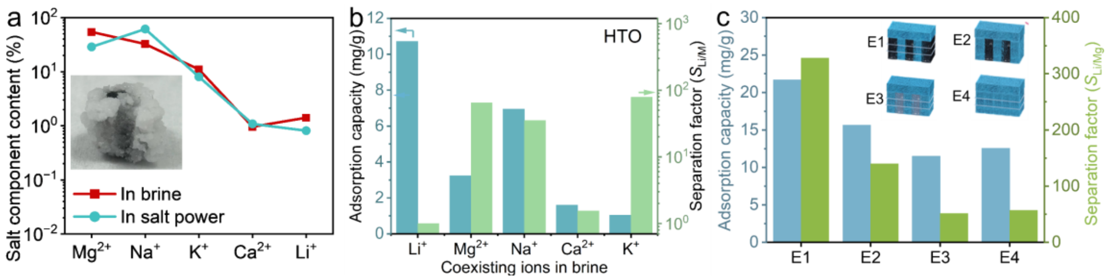

Fig. S26 Salt composition and adsorption analysis of control samples. (a) Precipitated salt composition on the surfaces of the evaporator composed of pristine sponge and CCH in dealing with salt-lake brine. (b and c) Adsorption capacity and separation factor of (b) pure HTO and (c) evaporators of various configurations in dealing with salt-lake brine (1 sun).

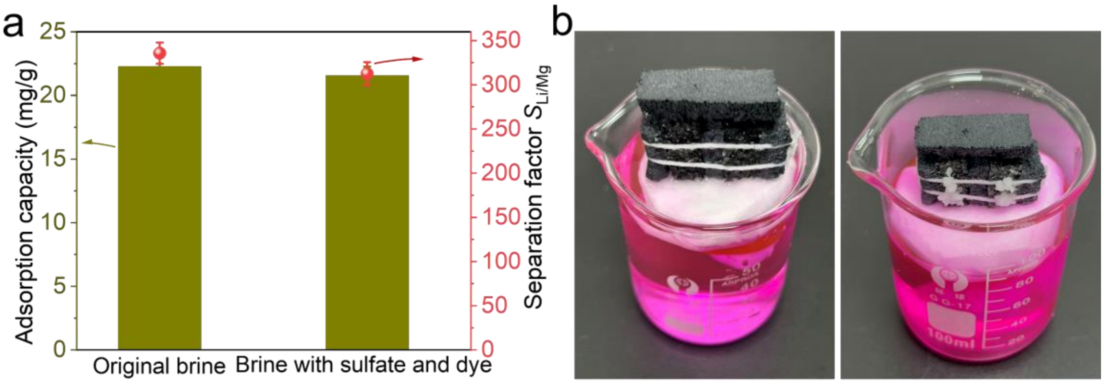

Fig. S27 (a) Lithium adsorption capacity and separation factor in brine with and without high concentration of sulfate (3.19 g/L) and dye (50 ppm). (b) Images showing the site-selective salt crystallization in 3D evaporator when dealing with brine of high concentration of sulfate and dye.

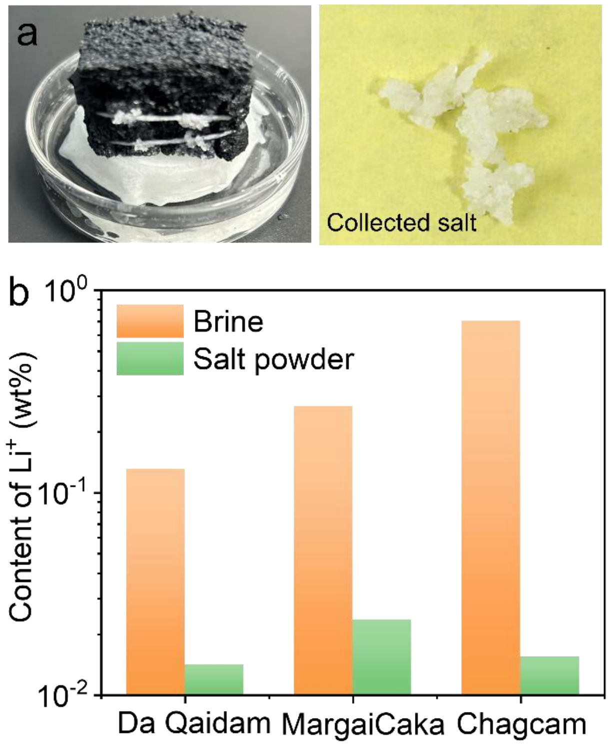

Fig. S28 (a) Images of the 3D evaporator with precipitated salt and the collected salt (b) The content of Li^+ in brine and salt powders collected from hydrophilic cotton thread of the 3D evaporator.

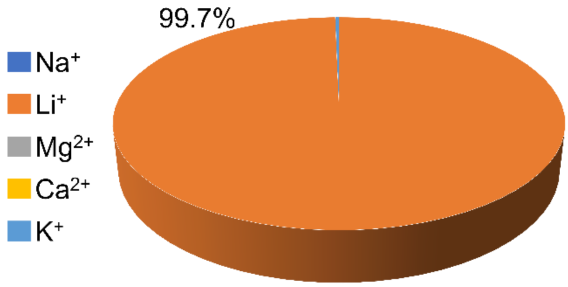

Fig. S29 Proportion of Na^{+}, Li^{+}, Mg^{2+}, Ca^{2+} and K^{+} in the collected Li_2CO_3.

Supplementary Tables

Table S1 Solar evaporation performance of the 3D evaporator in salty water compared with recent literature reports.

Entry	Photothermal material	Evaporation rate ($kg\ m^{-2}\ h^{-1}$)	Salinity (wt.%)	Reference
1	3D evaporator	3.04	20	This work
2	3D evaporator	3.145	0	This work
3	α-MoC_{1-x}@CB-based evaporator	2.8	3.5	1
4	α-MoC_{1-x}@CB-based evaporator	2.8	20	1
5	α-MoC_{1-x}@CB-based evaporator	2.8	0	1
6	Zinc-assisted WSE evaporator	1.43	0	2
7	Zinc-assisted WSE evaporator	1.25	10	2
8	Titanium mesh-based SVGC	0.62	0	3
9	Titanium mesh-based SVGC	1.22	3.5	3
10	Titanium mesh-based SVGC	0.56	7	3
11	Titanium mesh-based SVGC	0.54	12	3
12	Titanium mesh-based SVGC	0.48	17	3
13	Self-assembled aluminum nanoparticles	0.93	2.75	4
14	Self-assembled aluminum nanoparticles	1.26	3.5	4
15	Filter paper-CNTs	1.05	3.5	5
16	CuS-coated PE membrane	1.02	0	6
17	Copper-silicon nanowire porous membrane	0.81	3.5	7
18	Ppy-coated Hydrophilic PVDF membrane	0.92	3.5	8
19	Janus vertically oriented porous membranes	1.08	20	9
20	Janus SiO_2/cellulose nanofiber/carbon nanotube	1.2	3.5	10

21	Poly-pyrrole and polyvinyl alcohol (ppy/PVA)	1.09	3.5	11
22	3D Hydrogel Evaporator	2.26	3.5	12
23	3D Hydrogel Evaporator	2.23	10	12
24	3D Hydrogel Evaporator	2.15	15	12
25	3D Hydrogel Evaporator	1.95	20	12
26	Loofah and Co-MOF sponge	1.77	3.5	13
27	Loofah and Co-MOF sponge	1.769	10	13

Table S2 Compositions of China's three major salt lakes.

	Li^+ (g L^{-1})	Mg^{2+} (g L^{-1})	Na^+ (g L^{-1})	K^+ (g L^{-1})	Ca^{2+} (g L^{-1})	Mg^{2+}:Li^+ ratio	Total salinity (g L^{-1})
Da Qaidam	0.162	18.780	102.600	1.860	0.288	115.926	339.723
MargaiCaka	0.319	13.029	100.320	5.630	0.498	40.843	320.128
Chagcam Caka	0.893	15.550	79.351	6.364	0.110	17.413	334.059

Table S3 Parameters for Langmuir and Freundlich models for lithium adsorption of 3D evaporator.

Thermodynamic model	Parameters	1 sun irradiation
Langmuir	Q_m (mg g^{-1})	56.56
	k_L (L mg $^{-1}$)	0.00456
	R^2	0.993
Freundlich	k_F (mg g^{-1})	48.15
	n	0.92
	R^2	0.973

Table S4 Parameters for pseudo-first-order and pseudo-second-order models for lithium adsorption of the 3D evaporator under various conditions.

Kinetic models	Parameters	Adsorption conditions	
		Dark	1 sun irradiation
Pseudo-first-order	q_e (mg g^{-1})	15.26	26.94
	k_1 (min^{-1})	0.0087	0.0192
	R^2	0.979	0.970
Pseudo-second-order	q_e (mg g^{-1})	18.56	30.03
	k_2 (g min^{-1} mg^{-1})	5.16×10^{-4}	9.48×10^{-4}
	R^2	0.991	0.993

Table S5 Parameters for pseudo-first-order and pseudo-second-order models for lithium adsorption of evaporator composed of CH and O-Sponge under various conditions.

Kinetic models	Parameters	Adsorption conditions
		1 sun irradiation
Pseudo-first-order	q_e (mg g^{-1})	19.59
	k_1 (min^{-1})	0.00857
	R^2	0.988
Pseudo-second-order	q_e (mg g^{-1})	24.56
	k_2 (g min^{-1} mg^{-1})	3.52×10^{-4}
	R^2	0.991

Table S6 The calculated thermodynamic parameters of Li^+ adsorption by 3D evaporator.

ΔH (kJ mol^{-1})	ΔS (J mol K^{-1})	ΔG (kJ mol^{-1})			
		293 K	303 K	313 K	323 K
14.29	85.30	-10.72	-11.57	-12.42	-13.28

Table S7 Compositions of LiCl-$MgCl_2$ mixtures with a fixed salinity of 50.0 g L^{-1} and varying Mg^{2+}/Li^+ ratios.

Mg^{2+}: Li^+ ratio of solution	LiCl concentration (mg/L)	Li^+ concentration (mg/L)	$MgCl_2$ concentration (mg/L)	Mg^{2+} concentration (mg/L)	Total salinity (mg/L)
1	30536	5000	19587	5000	50000
10	6810	1115	43678	11150	
20	3634	595	46616	11900	
40	1893	310	48575	12400	
80	965	158	49515	12640	
160	489	80	50141	12800	

Table S8 Compositions of LiCl-$MgCl_2$ mixtures with a fixed Mg^{2+}/Li^+ ratio of 50 and varying salinities.

Total salinity (mg/L)	LiCl concentration (mg/L)	Li^+ concentration (mg/L)	$MgCl_2$ concentration (mg/L)	Mg^{2+} concentration (mg/L)	Mg^{2+}: Li^+ ratio of solution
200	6.11	1	195.87	50	
500	15.27	2.5	489.66	125	
1200	38.17	6.25	1224.16	312.5	
2500	76.34	12.5	2448.31	625	
5000	152.68	25	4896.63	1250	50
12000	381.70	62.5	12241.57	3125	
25000	763.40	125	24483.13	6250	
40000	11450.98	200	367246.97	10000	
50000	1526.80	250	195.87	12500	

Table S9 Comparison of solar evaporation performance, lithium adsorption performance and selectivity of the evaporators reported in the literature.

Adsorption material	Evaporation rate ($kg/m^2/h$)	Evaporation efficiency (%)	Mg^{2+}/Li^+ ratio	Lithium adsorption	$S_{Li/Mg}$	Reference
3D evaporator	3.14	91.33	116	20.26	503.2	This work
PAN/HMO	3.51	N/A	1	25.1	138	14
HTO/NMC/PS	1.29	90	13.38	12.1	160.5	15
PES/membrane	0.95	N/A	19.3	N/A	66	16
Al film	1.28	90	10	12.5	3.2	17

Table S10 Parameters for pseudo-first-order model for lithium adsorption of 3D evaporator in outdoor.

Kinetic models	Parameters	Adsorption conditions
		Outdoor
Pseudo-second-order	q_e (mg g^{-1})	29.56
	k_2 (g min^{-1} mg^{-1})	1.40×10^{-2}
	R^2	0.997

Table S11 Cost for the preparation of 3D evaporator.

Component		Unit Price ($/mt)	Mass per m^3 of Evaporator (kg)	Cost ($)
Hydrogel	PVA	~1404.49	25.84	36.29
	H_2TiO_3	~1685.39	4.08	6.88
	CB	~1685.39	4.08	6.88
	HCl	~70.22	1.133	0.08
	Glutaraldehyde	~2808.99	3.40	9.55
Hydrophobic sponge		42.13/m^3	0.32 m^3	13.48
Cotton thread		0.001756/m	8 m	0.014
Total materials cost				73.17/m^3

Table S12 Economic analysis of the production cost of Li_2CO_3 using the 3D evaporation system.

I. Capital Expenditure (CAPEX) Breakdown

Investment Item	Unit Price ($)	Quantity	Unit	Total Price ($)
		1. Evaporation Module		
Standardized Collection Cover	~210.67	5621	set	1184159.83
Support Frame and Water Distribution System	~42.13	5621	set	236831.97
		2. Core Process Equipment		
Bipolar Membrane Electrodialysis (BPED) System	~112359.55	1	set	112359.55
Initial Concentrated HCl Fill	~70.22	35.65	ton	2503.34
Various Solution Storage Tanks	~1685.39	2	unit	3370.78
		3. Auxiliary Systems		
Quantitative Control System	~11235.96	2	set	22471.91
Automatic Control System	~2106.74	1	set	2106.74
Total Capital Investment				**1563804.12**

II. Operating Cost Analysis (per ton of LCE, Production:1000 mt/yr)

Cost Item	Cost ($/mt)
A. Material Costs	
Evaporator Agent	3393.26
HCl	82.58
Na_2CO_3	519.10

Subtotal Material Cost	**3994.94**
B. Fixed Operating Costs (OPEX)	
Labor	101.12
Equipment Maintenance	31.28
Equipment Depreciation	156.32
Subtotal Fixed OPEX	**288.72**
C. Total Cost	**4283.66**

Table S13 Comparison of the Li_2CO_3 production cost with that reported in the literature.

Entry	Composition	Methods	Cost ($/mt LCE)	Reference
1	Evaporator	Litium adsorption	4283.66	This work
2	PHF-20 Particle	Litium adsorption	7556.18	18
3	HMO/PS Particle	Litium adsorption	7373.60	19
4	EP/HMO Particle	Litium adsorption	10372.47	20
5	-	Solvent exchange	12265.17	21
6	-	Membranes	4700-6200	22
7	-	Solar evaporation	5500-7000	22
8	Global Lithium Projects	Industry average	12815.73-15379.21	23

Supplementary Notes

Note S1 COMSOL simulation of the temperature distribution

The simulated 3D models were established based on the actual evaporation system, which mainly consisted of CCH hydrogel, O-Sponge, foam, and bulk water. The upper cuboid (15 mm ×10 mm×13 mm) composed of five vertically arranged cuboid units, (i.e., three pieces of CCH hydrogels and two pieces of O-Sponges in alternating row (3 mm × 10 mm × 10 mm)), and a horizontally covered cuboid layer (15 mm × 10 mm × 3 mm) was the 3D evaporator. The middle cylinder with height of 5 mm and radius of 11 mm was the floating PS foam, and the rest of whole cylinder with height of 10 mm and radius of 11 mm was the bulk water. The temperature distribution in the COMSOL model was described as the following equations:

$$E_{in} = \rho C_p \frac{\partial p}{\partial t} + \rho C_p u \cdot \nabla T + \nabla \cdot q \tag{S7}$$

$$q = -k \nabla T \tag{S8}$$

where E_{in} is the thermal energy input from the solar irradiation; x and t are the space vector and time, respectively; ρ, C_{p} and k are the mass density, specific thermal capacity, and thermal conductivity of the matters, respectively; T (x, t) refers to the local temperature and u is the fluid flow speed of the aqueous medium.

The theoretical simulation was performed by COMSOL Multiphysics under the steady-state analysis mode. The environment temperature was set to 293.15 K, and the heat convection between the upper surface of evaporator and air was corrected by Newton's law of cooling. The thermal conductivity, density, and specific thermal capacity of CCH are 0.0596 W m^{-1} K^{-1}, 356.9 kg m^{-3}, and 473 J kg^{-1} K^{-1}, respectively. The thermal conductivity, density, and specific thermal capacity of O-Sponge are 0.0594 W m^{-1} K^{-1}, 40 kg m^{-3}, and 17756 J kg^{-1} K^{-1}, respectively.

Note S2 Lithium adsorption mechanism

To determine the maximum capacities of the evaporator and to elucidate the adsorption behaviors, the widely used Langmuir (Equation S9) and Freundlich models (Equation S10) were employed. In these equations, q_m (mg g^{-1}) is the maximum adsorption capacity, K_L (L mg $^{-1}$) is the Langmuir constant, which pertains to the adsorption energy. Meanwhile, K_F (mg g^{-1}) and n are Freundlich constants for the adsorption capacity and adsorption intensity, respectively.

$$\frac{c_e}{q_e} = \frac{1}{q_m K_L} + \frac{c_e}{q_m} \tag{S9}$$

$$\text{In } q_e = \text{In } K_F + \frac{1}{n} \text{In } c_e \tag{S10}$$

Note S3 Lithium adsorption kinetics

The lithium adsorption kinetic data were fitted using pseudo-first order kinetic model and pseudo-second-order kinetic model where k_1 (min^{-1}) and k_2 (g mg^{-1} min^{-1}) are the rate constants of the pseudo-first-order and pseudo-second-order kinetic models, respectively. q_e and q_t are the amount of lithium (mg g^{-1}) adsorbed at equilibrium and at a certain time (t, min), respectively.

$$\text{In}\left(q_e\text{-}q_t\right) = \text{In} q_e - k_1 t \tag{S11}$$

$$\frac{t}{q_t} = \frac{1}{k_2 q_e^2} + \frac{t}{q_e} \tag{S12}$$

Note S4 Thermodynamics of lithium adsorption by 3D evaporator

The thermodynamic parameters of lithium adsorption by 3D evaporator were calculated according to the following equations:

$$InK_d = \frac{\Delta S}{R} - (\frac{\Delta H}{R})\frac{1}{T} \quad \text{(S13)}$$

$$K_d = \frac{c_0 - c_e}{c_e} \times \frac{V}{m} \quad \text{(S14)}$$

$$\Delta G = \Delta H - T\Delta S \quad \text{(S15)}$$

where K_d is the thermodynamic equilibrium coefficient (mL g^{-1}), ΔS is the standard entropy change (J mol^{-1} K^{-1}), ΔH is the standard enthalpy change (kJ mol^{-1}), R is the ideal gas constant (8.314 J mol^{-1} K^{-1}), T is the temperature of water (K), and ΔG is the standard Gibbs free energy (kJ mol^{-1}).

In the extraction of lithium from brine, the presence of functional groups in the adsorbent and the temperature are two key factors affecting the efficiency of lithium adsorption. According to the law of mass action and the Arrhenius formula:

$$v = k \times C_m^M \times C_n^N \quad \text{(S16)}$$

$$k = A \times e^{-\frac{Ea}{RT}} \quad \text{(S17)}$$

where v is the reaction rate, k is the reaction rate constant at the temperature T; C_M and C_N are the initial concentrations of the substrates M and N, while m and n are the chemical equilibrium coefficients of the substances M and N, respectively; A is the Arrhenius constant, and E_a is the experimental activation energy, which can be considered as a temperature-independent constant; R is the molar gas constant, and T is the temperature during the reaction. Therefore, increasing the lithium concentration and ambient temperature can lead to the enhanced coordination between lithium ions and the adsorbent material.

Note S5 COMSOL simulation of salt transport and crystallization

To investigate the salt transport and accumulation behavior in 3D photothermal evaporators with and without hydrophilic cotton threads (i.e., directional salt crystallization), time-dependent numerical simulations were conducted using COMSOL Multiphysics. Two evaporator models were constructed: one equipped with hydrophilic cotton threads contact with patterned hydrophilic and hydrophobic surfaces, and one without such threads. In both models, the top evaporation surface was modeled as an outlet to represent solar-driven evaporation, while the bottom water reservoir was treated as an inlet for continuous water supply (Fig. S29). To reflect the experimentally observed localized salt crystallization on the hydrophilic cotton threads, a small outlet boundary was defined at the midpoint of the thread in the simulation. Although this region is not directly exposed to solar irradiation, it consistently acts as a crystallization hotspot due to enhanced local evaporation driven by directed water transport, heat conduction from adjacent hydrophobic surfaces, and efficient vapor removal. Evaporation is simplified via imposed outlet boundary conditions, informed by experimental salt crystallization locations. It provides a physically reasonable approximation that captures the dominant salt transport and accumulation behavior. The hydrogel matrix was approximated as a continuous aqueous phase, as its porous structure exerts limited influence on the macroscopic transport dynamics of interest. Thus, the Laminar Flow module (LF) was used to solve for steady water movement within the porous structure, assuming incompressible, low-Reynolds-number flow. For the water flow numerical node, the equations are:

$$\rho \frac{\partial u}{\partial t} + \rho(u \cdot \nabla)u = \nabla \cdot (-pI + K) + F \tag{S18}$$

$$\frac{\partial \rho}{\partial t} + \nabla \cdot \rho u = 0 \tag{S19}$$

where ρ (SI unit: kg/m³) is the fluid density, and u (SI unit: m/s) is the fluid velocity vector. $\frac{\partial u}{\partial t}$ (SI unit: m/s²) is the local (temporal) acceleration of the fluid. p (SI unit: Pa = N/m²) is the pressure field, representing isotropic mechanical stress. I (dimensionless) Identity tensor. K (SI unit: Pa) is the viscous stress tensor. F (SI unit: N/m³) is the external body force.

Salt transport was governed by the Transport of Diluted Species (TDS) module, which accounted for both advection by the water flow and diffusion within the liquid phase. For the ion transport numerical node, the equations are:

$$\frac{\partial c_i}{\partial t} + \nabla \cdot J_i + u \cdot \nabla c_i = R_i \tag{S20}$$

$$J_i = -D_i \nabla c_i \tag{S21}$$

c_i (SI unit: mol/m^3) is the concentration of species i. u (SI unit: m/s) is the fluid velocity vector. J_i (SI unit: mol/m^2·s) is the diffusion flux. D_i (SI unit: m^2/s) is the diffusion coefficient of species i. R_i (SI unit: mol/m^3·s) is the net source or sink term and is the contribution from any generation, or consumption of species i.

Environmental parameters were set to match experimental conditions: an initial water temperature of 297.65 K. No-slip boundaries were applied at all solid-liquid interfaces, and the salt concentration at the inlet was set constant throughout the simulation. The simulation outputs revealed distinct differences in salt behavior with time between the two systems. In the evaporator without cotton threads, the highest salt concentration appeared near the center of the top evaporation surface, but the increase remained moderate and broadly distributed. In contrast, the thread-assisted evaporator showed sharp and localized salt accumulation surrounding the designated outlet region on the threads, indicating that guided water transport and preferential crystallization significantly alter salt distribution and flow direction in the system. Since the 3D simulation geometry made it difficult to clearly visualize ion transport using flow vectors due to the complexity of three-dimensional vector fields, a 2D planar model was constructed under the same physical assumptions and boundary conditions. This 2D simulation using identical material parameters, was solely used to better illustrate the ion migration pathways within the brine. The simplified geometry allowed clear visualization of ion transportation during evaporation in different evaporators, aiding the interpretation of the underlying transport mechanisms observed in the full 3D simulation.

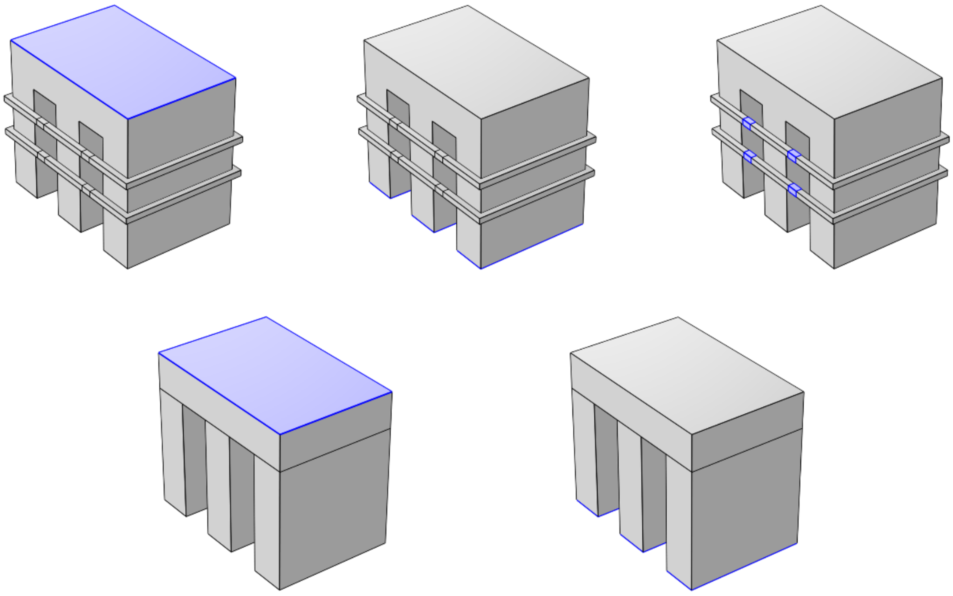

Fig. S30 Detailed model geometries and boundary setting in numerical simulations of salt transport and accumulation.

Note S6 Quality of the condensed water

(1) Solar evaporation of RhB or MB-polluted water and the collected condensed water

2.5 mg of RhB or MB powder was added to 50 mL of deionized water, and was stirred vigorously to obtain 50 ppm RhB or MB-polluted water. The concentration of RhB and MB was assessed by UV-Vis absorption spectrometer (UV6100).

(2) Solar evaporation of brine and the collected condensed water

The change in the concentration of ions was measured using inductively coupled plasma emission spectrometer (Thermo ICAP PRO, USA).

(3) Hemolysis ratio of various water samples

1 mL of 2% sheep erythrocyte solution was taken, centrifuged at 2000 rpm for 3 min, after which the supernatant was removed and the precipitate was added with 1 mL of 1 PBS solution for follow-up experiments.

0.2 mL of ultra-pure water, 0.2 mL of 1 PBS solution, 0.2 mL of brine, and 0.2 mL of distilled water were separately added to four tubes of the erythrocyte solution mentioned above. Then, 0.1 mL of the mixture was taken from each tube and transferred into another clean centrifuge tube, followed by addition of 0.9 mL of ultra-pure water. Then the mixture was incubated at 37 °C for 3 h to allow the erythrocytes to precipitate. The absorbance (A) of each group was measured at 540 nm using a UV-Vis spectrometer (UV6100). The hemolysis rate was calculated by the following equation:

$$\text{Hemolysis rate}(\%)=\frac{A_{Sample}-A_{PBS}}{A_{H_2O}-A_{PBS}} \tag{S22}$$

References

1. L. Zhu, L. Sun, H. Zhang, H. Aslan, Y. Sun, Y. Huang, F. Rosei and M. Yu, *Energy Environ. Sci.*, 2021, **14**, 2451-2459.
2. Y. Wang, T. Wei, Y. Wang, J. Zeng, T. Wang, Q. Wang, S. Zhang, M. Zeng, F. Wang and P. Dai, *Sci. Adv.*, 2024, **10**, eadk1113.
3. L. Yang, G. Chen, N. Zhang, Y. Xu and X. Xu, *ACS Sustainable Chem. Eng.*, 2019, **7**, 19311-19320.
4. L. Zhou, Y. Tan, J. Wang, W. Xu, Y. Yuan, W. Cai, S. Zhu and J. Zhu, *Nat. Photonics*, 2016, **10**, 393-398.
5. Y. Xia, Q. Hou, H. Jubaer, Y. Li, Y. Kang, S. Yuan, H. Liu, M. W. Woo, L. Zhang, L. Gao, H. Wang and X. Zhang, *Energy Environ. Sci.*, 2019, **12**, 1840-1847.
6. M. Shang, N. Li, S. Zhang, T. Zhao, C. Zhang, C. Liu, H. Li and Z. Wang, *ACS Appl. Energy Mater.*, 2017, **1**, 56-61.
7. X. Song, H. Song, N. Xu, H. Yang, L. Zhou, L. Yu, J. Zhu, J. Xu and K. Chen, *J. Mater. Chem. A*, 2018, **6**, 22976-22986.
8. Y. Wang, C. Wang, X. Song, M. Huang, S. K. Megarajan, S. F. Shaukat and H. Jiang, *J. Mater. Chem. A*, 2018, **6**, 9874-9881.
9. H.-H. Yu, L.-J. Yan, Y.-C. Shen, S.-Y. Chen, H.-N. Li, J. Yang and Z.-K. Xu, *Research*, 2020, **2020**, 11.
10. R. Hu, J. Zhang, Y. Kuang, K. Wang, X. Cai, Z. Fang, W. Huang, G. Chen and Z. Wang, *J. Mater. Chem. A*, 2019, **7**, 15333-15340.
11. Y. Shao, J. Tang, N. Li, T. Sun, L. Yang, D. Chen, H. Zhi, D. Wang, H. Liu and G. Xue, *EcoMat*, 2020, **2**, 12018.
12. L. Li, N. He, B. Jiang, K. Yu, Q. Zhang, H. Zhang, D. Tang and Y. Song, *Adv. Funct. Mater.*, 2021, **31**, 2104380.
13. H. Wang, C. Zhang, Z. Zhang, B. Zhou, J. Shen and A. Du, *Sol. RRL*, 2021, **5**, 2000817.
14. H.-N. Li, C. Zhang, J.-H. Xin, Y.-W. Liu, H.-C. Yang, C.-Y. Zhu, C. Liu and Z.-K. Xu, *ACS Nano*, 2024, **18**, 2434-2445.
15. Q. Xia, Z. Deng, S. Sun, W. Zhao, J. Ding, B. Xi, G. Gao and C. Wang, *Proc. Natl. Acad. Sci. U.S.A.*, 2024, **121**, e2400159121.
16. S. Zhang, X. Wei, X. Cao, M. Peng, M. Wang, L. Jiang and J. Jin, *Nat. Commun.*, 2024, **15**, 238.

17. Y. Song, S. Fang, N. Xu, M. Wang, S. Chen, J. Chen, B. Mi and J. Zhu, *Science*, 2024, **385**, 1444-1449.

18. S. Ding, W. Xing, L. Chen, L. Fu, X. Zhang, Z. Luo, Q. Li, M. Qin, J. Gong, J. Qu and R. Niu, *Chem. Eng. J.*, 2025, **522**, 167728.

19. J. Wang, W. Tang, M. Yang, Y. Yin, H. Li, F. Hu, L. Tang, X. Ma, Y. Zhang and Y. Wang, *Biomaterials*, 2021, **273**, 120784.

20. X. Lai, Y. Yuan, Z. Chen, J. Peng, H. Sun and H. Zhong, *Industrial & Engineering Chemistry Research*, 2020, **59**, 7913-7925.

21. I. Warren, *Techno-economic analysis of lithium extraction from geothermal brines*, National Renewable Energy Lab.(NREL), Golden, CO (United States), 2021.

22. M. Golmohammadi, Y. Boroumand, F. Arshadi, M. Asadnia and A. Razmjou, *Industrial & Engineering Chemistry Research*, 2025, **64**, 11113-11128.

23. M. Fleming, S. G. Kannan and R. Eggert, *Resour. Policy*, 2024, **97**, 105226.